https://doi.org/10.2352/ISSN.2470-1173.2019.9.IMSE-362

Spline-Based Colour Correction for Monotonic Nonlinear CMOS Image Sensors

Syed Hussain and Dileepan Joseph; University of Alberta; Edmonton, AB, Canada

Abstract

Nonlinear CMOS image sensor (CIS) technology is capable of high/wide dynamic range imaging at high frame rates without motion artifacts. However, unlike with linear CIS technology, there is no generic method for colour correction of nonlinear CIS technology. Instead, there are specific methods for specific nonlinear responses, e.g., the logarithmic response, that are based on legacy models. Inspired by recent work on generic methods for fixed pattern noise and photometric correction of nonlinear sensors, which depend only on a reasonable assumption of monotonicity, this paper proposes and validates a generic method for colour correction of nonlinear sensors. The method is composed of a nonlinear colour correction, which employs cubic Hermite splines, followed by a linear colour correction. Calibration with a colour chart is required to estimate the relevant parameters. The proposed method is validated, through simulation, using a combination of experimental data, from a monochromatic logarithmic CIS, and spectral data, reported in the literature, of actual colour filter arrays and target colour patches.

Introduction

CMOS image sensors (CISs) have become the dominant imaging technology, with CCDs comprising less than 10% of the market share since 2010 [1]. Research in the area includes work on nonlinear sensors, such as logarithmic (log) and linear-logarithmic (linlog) ones [2, 3]. It is well known they can achieve a high/wide dynamic range (DR) in single exposures at video rates and, with the work of Mahmoodi *et al.* [4], also to realize a high peak signal-to-noise-and-distortion ratio (PSNDR).

Recent work on nonlinear sensors does not address colour specifically. Brunetti and Choubey [2] alter the log sensor circuit to improve its sensitivity in the dark. Meanwhile, Bae *et al.* [3] develop a variation of the linlog circuit with two piecewise linear regions in the dark. Given that colour is an integral component of visible-band imaging technology, one can safely assume from the ongoing interest in nonlinear sensors that legacy work on colour correction in such sensors is worth improving upon.

The main limitation of legacy work on colour correction, in nonlinear sensors, is that it is specific to the classic log sensor. Methods by Hoefflinger [5] and Joseph and Collins [6] rely on a classic model of the log sensor, developed by Joseph and Collins [7] for fixed pattern noise (FPN) correction. While these colour correction methods worked to some degree, they are not applicable to the variety of nonlinear sensors of interest today, including log sensor variations that deviate from the classic model.

This paper proposes a new approach to colour correction, which leverages a model recently developed by Li *et al.* [8], using low-degree polynomials and cubic Hermite splines, for FPN and photometric correction. Relying only on the monotonicity of pixel responses, this model is so generic that it may be applied to a wide variety of sensors, including log and linlog variations. Also, Li *et al.* [8] showed that, when applied to Mahmoodi *et al.*'s log sensor [4], FPN correction using the generic model was competitive with FPN correction using the classic specific model.

One difficulty of working on this subject is the challenge of obtaining experimental data from a nonlinear image sensor, i.e., an array of nonlinear pixel sensors, having a colour filter array (CFA). Therefore, we adopt a simulation strategy here by using monochromatic experimental data, from Mahmoodi *et al.*'s documented image sensor [4], and spectral data from multiple literature sources, regarding the quantum efficiency (QE) of photodiodes, the transmittance of a CFA, and the reflectance of a wide variety of objects, to validate our proposed method.

We first summarize the apparatus of interest, i.e., a nonlinear sensor that obeys the assumptions laid out by Li *et al.* [8]. However, we extend Li *et al.*'s model from a monochromatic to a colour scenario. Thereafter, the new colour correction method is proposed, which entails a description also of colour calibration. Because FPN is inherent to nonlinear sensors and Li *et al.*'s model, we review FPN, its calibration, and its correction, focusing on implications for colour calibration and correction.

Moreover, we present a suite of results to validate and evaluate the proposed method, including two variations thereof. They include calibration with Macbeth chart patches and testing with a large database of other patches. Not only do we report median 1976 CIE L*a*b* (CIELAB) errors, including over a high/wide DR, but also their probability density functions (PDFs). Errors are broken down into luminance and chromaticity parts, and are compared to just noticeable difference (JND) thresholds.

We conclude the paper by summarizing our motivation, apparatus, methods, results, and discussion. Our conclusion also highlights the novelty and significance of this work—a generic method for the colour correction of nonlinear sensors.

Apparatus and Method

This paper proposes and validates a method to correct colour for the class of image sensors that are strictly nonlinear and monotonic in their response to incoming light. The method is intended to be implemented, in real time, as one subsystem in a series of subsystems of an image processing pipeline. It is designed to output images in the 1931 CIE XYZ (XYZ) colour space. These may be easily transformed into other colour spaces.

Figure 1 illustrates a nonlinear imaging system, comprising a nonlinear image sensor and an image processing pipeline for FPN and colour correction. A transformation to the sRGB colour space, suitable for display, is indicated at the output.

The proposed method has two stages. The first is calibration, which is performed once to establish parameters required in

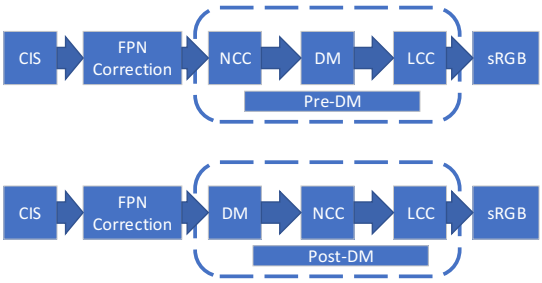

Figure 1. *The proposed colour imaging system. Dashed boxes indicate the focus of our work. Nonlinear colour correction (NCC) is done before or after demosaicing (DM). They are followed by linear colour correction (LCC).*

the correction stage. Correction is then performed, in real time on all frames, using a combination of nonlinear and linear colour corrections. Assuming the image sensor uses a CFA, demosaicing is also needed. Variations in the sequence of performing the colour corrections and demosaicing yield different results.

Below, we first analyze relevant aspects of image sensors. Next, taking nonlinear and linear parts separately, the proposed colour correction method is explained, calibration included. For demosaicing, we simply use Malvar *et al.*'s [9] algorithm.

Image Sensor

An imaging system views an object when a spectrum of light reflects off a scene and hits an array of pixels. In a given pixel array, the circuit configuration of the pixels will not vary, but due to variations in device manufacturing, responses to identical input can vary from pixel to pixel. This is the basis of FPN.

Considering FPN and nonlinearity, to describe the response of the jth pixel, in an array of pixels, we can write:

$$y_j = f_j(x_j) + \varepsilon_j, \tag{1}$$

where f_j is the opto-electronic conversion function (OECF) of the pixel, ε_j is a noise associated with each pixel that encapsulates temporal and quantization noise, and x_j is the stimulus.

The stimulus x_j, of the jth pixel, depends on localized scene illumination and object reflectance, as well as CFA transmission and photodiode sensitivity. It can be modeled as follows:

$$x_j = \int_0^\infty s_j(\lambda)\beta_j(\lambda)\alpha_j(\lambda)d\lambda, \tag{2}$$

where s_j, β_j, and α_j, which are functions of wavelength λ, are the illumination, reflectance, and absorption spectra. Whereas x_j and s_j can have dimensions, e.g., cd/m^2 and cd/m^2/nm, β_j and α_j are always dimensionless and range from 0 to 1.

Assuming R, G, and B represent, according to the CFA, the sets of pixels with red, green, and blue colour filters, respectively, the absorption spectrum may be modeled as follows:

$$\alpha_j(\lambda) = \begin{cases} T_\mathrm{R}(\lambda)Q(\lambda), & j \in R, \\ T_\mathrm{G}(\lambda)Q(\lambda), & j \in G, \\ T_\mathrm{B}(\lambda)Q(\lambda), & j \in B, \end{cases} \tag{3}$$

where T_R, T_G, and T_B are the transmission efficiencies of the red, green, and blue colour filters, and Q is the quantum efficiency of the photodiode. They are treated as constants because there are enough degrees of freedom, in (1), to model FPN.

The proposed method requires that f_j, the OECF in (1), be a monotonic function. Monotonicity is a typical characteristic of any image sensor, including linear, log, and linlog. Although we use data from a log sensor, for validation purposes, the method is mathematically applicable to linlog and other possible high/wide DR sensors. The success of the method depends neither on the form of the OECF nor on its variation from pixel to pixel.

Nonlinear Correction

We assume FPN correction, shown in Fig. 1, is implemented using a polynomial-based method our lab previously published [8]. In that paper, our lab also introduced a spline-based method for photometric correction. We amend and extend those methods, in this paper, to realize a nonlinear colour correction.

Considering the pre-demosaicing variation, shown in Fig. 1, nonlinear colour correction follows FPN correction. During FPN calibration, an average response is computed as follows:

$$\bar{y}_i = \frac{1}{n}\sum_{j=1}^{n} y_{ij}, \tag{4}$$

where y_{ij} is the response to a uniform stimulus x_i, which varies, and n is the number of pixels. The averaging, in (4), reduces the significance of ε_j, in (1). The noise may be reduced further by averaging, for each stimulus x_i, over multiple frames.

Data points $(x_i, \bar{y}_i)$, from FPN calibration, are used to define F, an ideal monotonic and nonlinear OECF, as follows:

$$\bar{y}_i = F(x_i) \equiv \frac{1}{n}\sum_{j=1}^{n} f_j(x_i). \tag{5}$$

Our FPN calibration also computes n low-degree polynomials P_j, which are used to implement FPN correction as follows:

$$\hat{y}_j = P_j(y_j) \approx F(x_j), \tag{6}$$

where x_j and y_j are the stimulus and response, in (1), and $\hat{y}_j$ is the corrected response, i.e., the FPN correction output.

Our photometric correction computes an estimated stimulus, $\hat{x}_j$, using the corrected response, $\hat{y}_j$, as follows:

$$\hat{x}_j = \exp(S^{-1}(\hat{y}_j)) \approx F^{-1}(\hat{y}_j), \tag{7}$$

where S^{-1} is a cubic Hermite spline [10] fitted to the data points $(\ln x_i, \bar{y}_i)$ in the inverse direction. Logarithms are used to robustly deal with a high/wide DR on the x-axis. Unlike a cubic spline, a cubic Hermite spline guarantees monotonicity.

The stimulus x_i, in (5), is constant for all pixels, for a uniform scene imaged by a monochromatic sensor, because the absorption spectrum α_j equals the quantum efficiency Q, in (3). However, for a uniform scene imaged by a colour sensor, the stimulus must be represented by three constants, as follows:

$$x_i^\mathrm{R} = s_i \int_0^\infty s_0(\lambda)\beta(\lambda)T_\mathrm{R}(\lambda)Q(\lambda)d\lambda, \tag{8}$$

$$x_i^\mathrm{G} = s_i \int_0^\infty s_0(\lambda)\beta(\lambda)T_\mathrm{G}(\lambda)Q(\lambda)d\lambda, \tag{9}$$

$$x_i^\mathrm{B} = s_i \int_0^\infty s_0(\lambda)\beta(\lambda)T_\mathrm{B}(\lambda)Q(\lambda)d\lambda, \tag{10}$$

where s_0 is the normalized illumination spectrum, e.g., a D65 spectrum in $1/\text{nm}$, and s_i its photometric intensity, e.g., in cd/m^2. The R, G, or B superscripts indicate that the constants apply only to the red, green, or blue pixels, respectively.

Consequently, our previous FPN and photometric methods must be performed three times separately, once each for the red, green, and blue pixels. Instead of (6) and (7), we obtain:

$$\hat{y}_j = P_j(y_j) \approx \begin{cases} F_{\text{R}}(x_j), & j \in R, \\ F_{\text{G}}(x_j), & j \in G, \\ F_{\text{B}}(x_j), & j \in B, \end{cases} \tag{11}$$

$$\hat{x}_j = \begin{cases} \exp(S_{\text{R}}^{-1}(\hat{y}_j)) \approx F_{\text{R}}^{-1}(\hat{y}_j), & j \in R, \\ \exp(S_{\text{G}}^{-1}(\hat{y}_j)) \approx F_{\text{G}}^{-1}(\hat{y}_j), & j \in G, \\ \exp(S_{\text{B}}^{-1}(\hat{y}_j)) \approx F_{\text{B}}^{-1}(\hat{y}_j), & j \in B, \end{cases} \tag{12}$$

where F_{R}, F_{G}, and F_{B} are ideal monotonic and nonlinear OECFs for red, green, and blue pixels, respectively, and S_{R}, S_{G}, and S_{B} are the cubic Hermite splines for the same. The splines may easily be created in normal or inverse directions, as indicated.

Thus, for the pre-demosaicing variation, the nonlinear colour correction is given by (12). It operates directly on the result, given by (11), of FPN correction. Each scalar $\hat{x}_j$ represents either a red, green, *or* blue value. After demosaicing, using the established algorithm by Malvar *et al.* [9], for each pixel there is a red, green, *and* blue value, which we may represent by a vector $\hat{\mathbf{x}}_j$.

Alternately, for the post-demosaicing variation, shown in Fig. 1, demosaicing happens after FPN correction. The result of FPN correction is still a red, green, *or* blue scalar $\hat{y}_j$. It becomes a red, green, *and* blue vector $\hat{\mathbf{y}}_j$ after demosaicing. Thus, instead of (12), the nonlinear colour correction is as follows:

$$\hat{\mathbf{x}}_j = \begin{bmatrix} \exp(S_{\text{R}}^{-1}(\hat{y}_j^{\text{R}})) \\ \exp(S_{\text{G}}^{-1}(\hat{y}_j^{\text{G}})) \\ \exp(S_{\text{B}}^{-1}(\hat{y}_j^{\text{B}})) \end{bmatrix} \approx \begin{bmatrix} F_{\text{R}}^{-1}(\hat{y}_j^{\text{R}}) \\ F_{\text{G}}^{-1}(\hat{y}_j^{\text{G}}) \\ F_{\text{B}}^{-1}(\hat{y}_j^{\text{B}}) \end{bmatrix}, \tag{13}$$

where $\hat{y}_j^{\text{R}}$, $\hat{y}_j^{\text{G}}$, and $\hat{y}_j^{\text{B}}$ are components of the vector $\hat{\mathbf{y}}_j$. The end result is a vector $\hat{\mathbf{x}}_j$ for either variation in Fig. 1.

Linear Correction

The input of the linear colour correction, shown in Fig. 1, is always a tristimulus vector, denoted $\hat{\mathbf{x}}_j^{\text{RGB}}$, in the colour space of the nonlinear image sensor. Because nonlinear aspects are already corrected, the proposed linear colour correction proves identical to the colour correction of linear image sensors, i.e.,

$$\hat{\mathbf{x}}_j^{\text{XYZ}} = \hat{\mathbf{D}}^{-1} \hat{\mathbf{x}}_j^{\text{RGB}}, \tag{14}$$

where $\hat{\mathbf{x}}_j^{\text{XYZ}}$ is the corrected tristimulus vector, in the standard XYZ colour space, and $\hat{\mathbf{D}}$ is a 3×3 matrix, which is invertible, that represents the underlying linear relationship.

Therefore, the novelty here is not in linear colour correction per se but rather in its calibration process, i.e., how $\mathbf{D}$ is estimated, because that is different compared to the linear image sensor case. One part of the calibration process remains the same. We require an image y_j of a standard colour chart, e.g., a Macbeth chart, illuminated by a standard illuminant, e.g., D65. After segmenting the image to isolate the colour chart patches, the true XYZ values, $\mathbf{x}_j^{\text{XYZ}}$, of segmented pixels, $j \in C$, are known.

To estimate the unknown parameter $\mathbf{D}$, we minimize a sum of square errors (SSE), which is defined as follows:

$$SSE = \sum_{j \in C} (\hat{y}_j - Y_j)^2, \tag{15}$$

where $\hat{y}_j$ is the result, in (11), after FPN correction of the colour chart image y_j. For $j \in C$, Y_j is defined as follows:

$$Y_j = \begin{cases} S_R(\ln x_j^{\text{R}}) \approx F_R(x_j^{\text{R}}), & j \in R, \\ S_G(\ln x_j^{\text{G}}) \approx F_G(x_j^{\text{G}}), & j \in G, \\ S_B(\ln x_j^{\text{B}}) \approx F_B(x_j^{\text{B}}), & j \in B, \end{cases} \tag{16}$$

where S_R, S_G, and S_B are cubic Hermite splines that model ideal OECFs F_R, F_G, and F_B, as described previously, and x_j^{R}, x_j^{G}, and x_j^{B} are components of $\mathbf{x}_j^{\text{RGB}}$. Due to a final equation, i.e.,

$$\mathbf{x}_j^{\text{RGB}} = \mathbf{D} \mathbf{x}_j^{\text{XYZ}}, \tag{17}$$

the scalar SSE, in (15), depends on the matrix $\mathbf{D}$.

As all relevant functions are differentiable, the gradient of the SSE with respect to $\mathbf{D}$, denoted ∇SSE, may be formulated. Using an established algorithm, such as `fminunc` in MATLAB, which terminates when ∇SSE equals the zero matrix, the SSE may be minimized. The matrix $\hat{\mathbf{D}}$ that minimizes the SSE is then used, in (14), to implement the linear colour correction.

Results and Discussion

This section summarizes the results of testing the proposed method, and discusses the results achieved. First, we present details on how a colour nonlinear image sensor is simulated. Next, we describe how the image sensor is calibrated, and present the results of the calibration. Results of correction are then presented, including performance over a high/wide DR.

Image Sensor

The method is validated using a simulated colour log image sensor based on the model presented above. As with Li *et al.* [8], the OECF of the image sensor is determined by taking several images of uniform scenes of constant luminance.

Using literature data [11, 12], shown in Fig. 2, the stimulus x_j is simulated by evaluating (2) for each pixel, which has a colour filter on top of a photodiode, of the image sensor. The quantum efficiency $Q(\lambda)$ is a measure of the electron-hole pairs generated relative to photons, of a particular wavelength, incident on the photodiode. The colour filters are used to limit the wavelengths to a certain range and to weight them appropriately.

Assuming a standard Bayer CFA, we segment pixels into red ($j \in R$), green ($j \in G$), and blue ($j \in B$) sets. Using data from a monochromatic log image sensor, presented by Mahmoodi *et al.* [4], we compute red (S_R), green (S_G), and blue (S_B) cubic Hermite splines to model the ideal OECFs of red, green, and blue pixels, respectively, for colour calibration purposes. Inverse cubic Hermite splines are computed for colour correction.

As shown in Fig. 1, we focus on the colour correction part of a hypothetical nonlinear imaging system, in this case a log imaging system. Using Li *et al.*'s method, the FPN correction output, i.e., $\hat{y}_j$ in (6), is for each pixel equivalent to its ideal response, i.e., based on its ideal OECF, plus residual noise. According to Li *et*

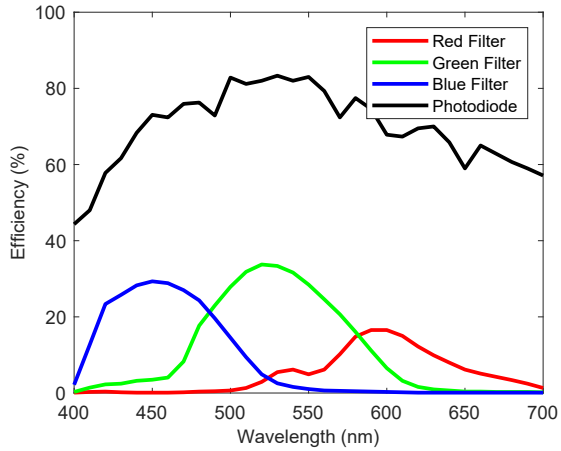

Figure 2. *Transmission and quantum efficiency data from the literature. Red, green, and blue transmission efficiencies correspond to a Canon 5D CFA. The photodiode quantum efficiency is from a standard CMOS process. We use this data to help simulate a colour nonlinear image sensor.*

al., the residual noise is proportional to the original noise ε_j, in (1), and is normally distributed with zero mean.

Consequently, for each pixel of our colour log image sensor, we simulate the response to the stimulus as follows:

$$\hat{y}_j = \begin{cases} \text{round}(S_R(x_j) + \varepsilon_j), & j \in R, \\ \text{round}(S_G(x_j) + \varepsilon_j), & j \in G, \\ \text{round}(S_B(x_j) + \varepsilon_j), & j \in B, \end{cases} \tag{18}$$

where ε_j is pseudo-random noise that is normally distributed, with a standard deviation that matches that of the original log image sensor. Responses are rounded, which introduces some quantization noise, because Li *et al.*'s FPN correction preserves the 16-bit integer format of Mahmoodi *et al.*'s image sensor.

Colour Calibration

Colour calibration is performed using the Macbeth chart, a standard colour chart consisting of 24 square patches [13]. Spectral information of each patch is known, along with its XYZ coordinates. Assuming 10×10 pixels per patch, we simulated the stimulus image of the Macbeth chart, the image after FPN correction, and the image after colour correction. This was done using the standard D65 illuminant at $10^4\,\text{cd}/\text{m}^2$.

The results of the calibration can be checked qualitatively by converting the true and corrected XYZ values to a displayable sRGB format [14], and then viewing them next to each other. Figure 3 illustrates the Macbeth chart, with the left half of each patch showing the corrected values, and the right half the true values. Due to simulated image sensor noise, the left halves exhibit a small pixel to pixel variation that cannot be seen.

To quantify errors, we use the CIELAB colour space due to its approximation of perceptual uniformity [15]. We convert true and corrected XYZ tristimulus values to CIELAB coordinates. Thereafter, the Euclidean distance, between the true and corrected CIELAB vectors, provides an estimate of perceived colour difference. It may be compared to a JND of 2.3 [16]. Although more accurate colour difference formulas exist, the Euclidean distance in CIELAB space was chosen because of its simplicity.

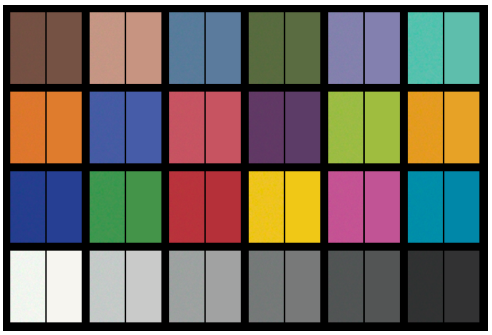

Figure 3. *True and corrected Macbeth chart in sRGB colour space. The right half of each patch shows the true colour, using the D65 illuminant at $10^4\,cd/m^2$, while each pixel in the left half shows its corrected colour, which varies imperceptibly due to noise, after calibration and correction.*

Table 1 gives the median correction error ΔE, over all $24 \times 10 \times 10$ pixels of the Macbeth chart patches, after the calibration and correction. Results for the chosen CFA are given, as well as for an ideal CFA that employs the XYZ spectral functions.

The closer the actual CFA spectral functions are to a linear combination of the ideal spectral functions, the better the results would be, even for linear imaging systems. An improvement of the results when an ideal CFA is used, as indicated in Table 1, means that non-idealities of the actual CFA play a limiting factor, irrespective of the nonlinear response of the image sensor.

Figure 4 presents a detailed comparison of true and corrected coordinates in CIELAB space. As six patches in the last row of the Macbeth chart have low a*-b* coordinates, they crowd near the origin of the chromaticity graph. While errors are primarily along the green-red axis, colour matching is good.

Recalling Fig. 1, two variations of the imaging system are considered: pre-demosaicing and post-demosaicing. Whereas the colour calibration process is the same for both, the impact of the variations may be analyzed, in CIELAB space after colour correction, using the Macbeth chart. In fact, median correction errors for both variations are reported in Table 1. These results imply that pre-demosaicing outperforms post-demosaicing.

Figure 5 shows the error after colour correction of the calibration image over a high/wide DR. Although illumination intensity is varied, the colour correction parameters are estimated only once, at $10^4\,\text{cd}/\text{m}^2$ as before. In addition to imaging system variations, results are shown for actual and ideal CFAs.

It is evident, in Fig. 5, that the pre-demosaicing method outperforms the post-demosaicing method at higher intensities. At lower intensities, however, the reverse is true. In any case, errors

Table 1. Median CIELAB error of the Macbeth chart image. Using the D65 illuminant, at $10^4\,\text{cd}/\text{m}^2$, the median error after colour calibration and correction was calculated. It was done for both system variations, in Fig. 1, and an ideal CFA.

Simulated CFA	ΔE (Pre-DM)	ΔE (Post-DM)
Canon 5D	0.8545	1.3860
Ideal XYZ	0.2441	0.3336

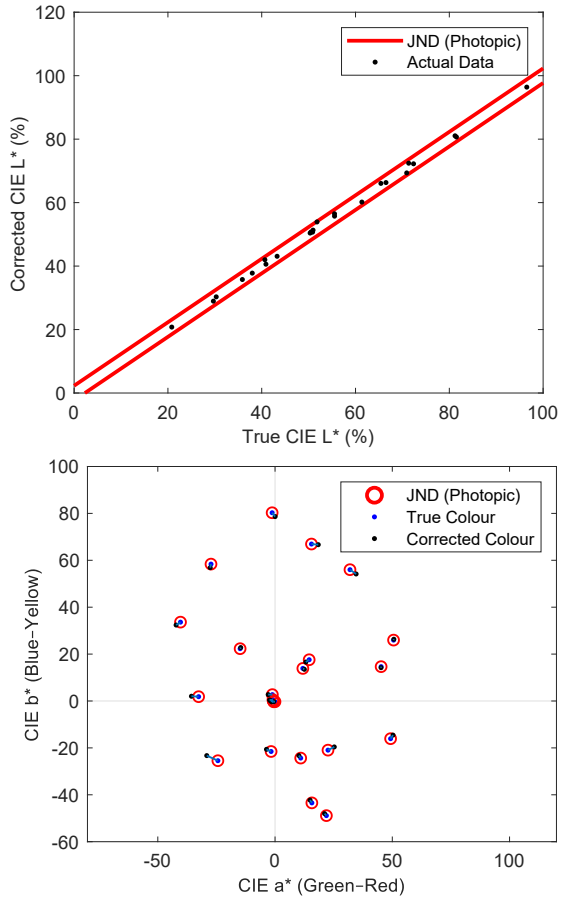

Figure 4. *Luminance and chromaticity errors of Macbeth chart patches. Red lines and circles in the luminance (top) and chromaticity (bottom) graphs indicate JND regions. Errors are computed after calibration and correction at 10^4 cd/m^2. Each corrected coordinate represents a typical pixel.*

are above the JND at lower intensities. While this is partly because of non-idealities of the CFA, it may also be affected by the relatively high dark limit of Mahmoodi *et al.*'s log image sensor [4], a topic that is beyond the scope of this work.

Colour Correction

To validate the proposed method properly, it is important to test colour correction on images that were not used for colour calibration. To this end, the Standard Object Color Spectra (SOCS), published by the International Organization for Standardization (ISO), was used [17]. This database contains reflectance spectra of over 50,000 objects divided into various categories.

The ISO suggests categories of data that are especially suited for evaluating digital cameras. They are called "human faces," "Krinov," which concerns buildings, "flowers," and "leaves." We used all 1,148 spectra, in these 4 categories, and simulated 10×10 pixel patches, as before. We focus on the pre-demosaicing variation of the imaging system, for simplicity, with the actual CFA. Finally, we used the 24 spectra of the Macbeth chart patches, for calibration purposes, and the same D65 illuminant.

Differences, between true and corrected colours, are quantified once again using the Euclidean distance in CIELAB space.

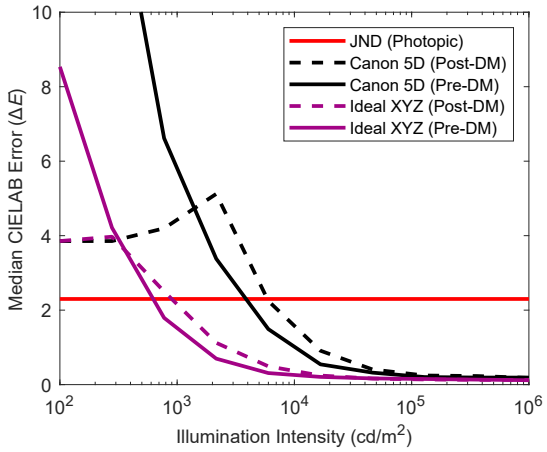

Figure 5. *Median CIELAB error per intensity of Macbeth chart images. Using the D65 illuminant, after calibration at 10^4 cd/m^2, the median error after colour correction was calculated at various intensities. Results are shown for both system variations, in Fig. 1, as well as for an ideal CFA.*

Table 2 reports the median error of all pixels in each category. Note that each patch has the same number of pixels.

Considering that the JND is 2.3 in CIELAB space, Table 2 demonstrates that the colour correction performs well, on median. Given the large number of images per category, compared to the 24 patches of the Macbeth chart, we can estimate a PDF across the images, per category, of the median error per image. Such a result provides a comprehensive assessment of colour correction, because a PDF determines all statistics of interest.

Figure 6 shows, for each category, the estimated PDF of the median error per image. The JND is also indicated. Errors vary the most for the flowers category, the only category with a significant error probability mass beyond the JND, even though the median error is better than that of the faces category.

Because the actual CFA was used in these results, its non-idealities are a limiting factor, as implied previously with Table 1. If transmission efficiencies of the red, green, and blue filters, multiplied by the quantum efficiency of the photodiode, were made to closely follow a linear combination of ideal XYZ matching functions, we would expect an improvement in the results.

Figure 7 shows the results of correction at varying intensities. As demonstrated, the colour correction proves stable enough for high/wide DR applications involving a large variety of objects. Future work will investigate how to improve performance at dimmer intensities. Possibilities include the improvement of

Table 2. Median CIELAB error of simulated SOCS images. The median error after colour correction was calculated using the D65 illuminant at 10^4 cd/m^2, after colour calibration using a Macbeth chart imaged under the same illumination.

Category	Images	ΔE
Faces	538	1.6440
Buildings	370	1.1273
Flowers	148	1.5242
Leaves	92	1.1379

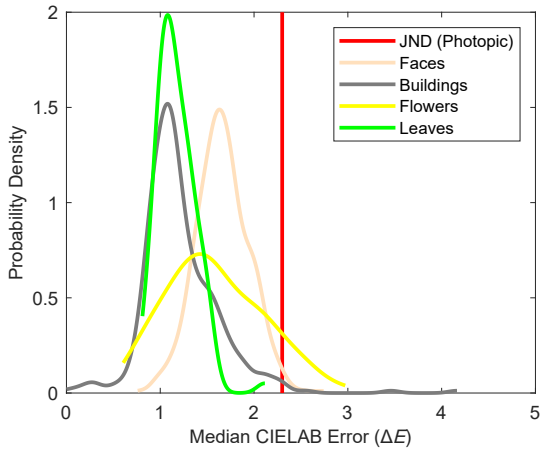

Figure 6. *The PDF of median CIELAB error of simulated SOCS images. Each SOCS category has enough images to estimate the PDF reasonably well. All correction is performed, using the D65 illuminant at 10^4 cd/m^2, after calibration using a Macbeth chart imaged with the same illumination.*

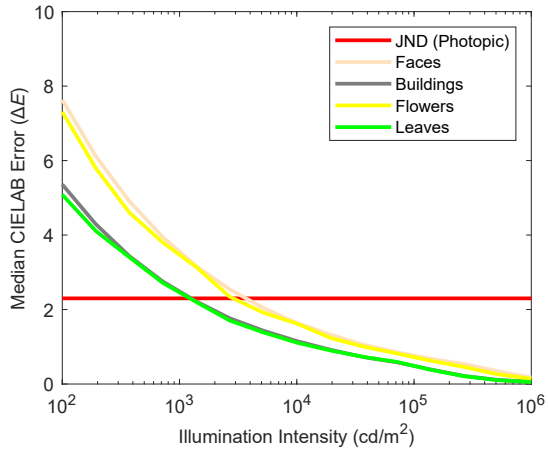

Figure 7. *Median CIELAB error per intensity of simulated SOCS images. The median error after colour correction, using the D65 illuminant at various intensities, was calculated for each SOCS category, after colour calibration using a Macbeth chart imaged with the same illuminant at 10^4 cd/m^2.*

the colour filters and dark limit of the image sensor.

Conclusion

This paper proposed a novel method for colour correction of nonlinear CMOS image sensors, which are ideal for high/wide DR applications. The method is neither limited by the specific nonlinear response, i.e., the specific OECF, of the image sensor, nor by FPN, i.e., a variation of the OECF from pixel to pixel due to device mismatch. The only requirement of the method is that the OECF be a monotonic function of light stimulus.

The monotonic property of the OECF allows for cubic Hermite splines to be constructed to allow calibration and correction of red, green, and blue pixel responses. As with linear imaging systems, a 3×3 matrix is also involved. Colour correction is done after FPN correction using Li *et al.*'s method [8], also from our research group. The two methods are complementary and both are needed to realize a colour nonlinear imaging system.

Validation is done by simulating a colour log image sensor using data collected in previous works. This image sensor is used to image a standard Macbeth chart, for colour calibration and its validation, and 1,148 standard objects, for colour correction and its validation. Results show that the proposed method performs well, relative to the JND when errors are measured in CIELAB space, for a large variety of standard objects.

References

[1] P. Cambou and J.-L. Jaffard, "Status of the CMOS Image Sensors Industry," techreport, Yole Développment, 2015.

[2] A. M. Brunetti and B. Choubey, "A low dark current wide dynamic range CMOS pixel," in *IEEE International Symposium on Circuits and Systems*, pp. 2523–2526, 2016.

[3] M. Bae, B.-S. Choi, S.-H. Jo, H.-H. Lee, P. Choi, and J.-K. Shin, "A Linear-Logarithmic CMOS Image Sensor With Adjustable Dynamic Range," *IEEE Sensors Journal* **16**(13), pp. 5222–5226, 2016.

[4] A. Mahmoodi, J. Li, and D. Joseph, "Digital Pixel Sensor Array with Logarithmic Delta-Sigma Architecture," *Sensors* **13**(8), pp. 10765–10782, 2013.

[5] B. Hoefflinger, *High-Dynamic-Range (HDR) Vision*, vol. 26 of *Advanced Microelectronics*, Springer, 2007.

[6] D. Joseph and S. Collins, "Modeling, calibration, and rendition of color logarithmic CMOS image sensors," *IEEE Transactions on Instrumentation and Measurement* **52**(5), pp. 1581–1587, 2003.

[7] D. Joseph and S. Collins, "Modeling, calibration, and correction of nonlinear illumination-dependent fixed pattern noise in logarithmic CMOS image sensors," *IEEE Transactions on Instrumentation and Measurement* **51**(5), pp. 996–1001, 2002.

[8] J. Li, A. Mahmoodi, and D. Joseph, "Using Polynomials to Simplify Fixed Pattern Noise and Photometric Correction of Logarithmic CMOS Image Sensors," *Sensors* **15**(10), pp. 26331–26352, 2015.

[9] H. S. Malvar, L.-w. He, and R. Cutler, "High-quality linear interpolation for demosaicing of Bayer-patterned color images," in *IEEE International Conference on Acoustics, Speech, and Signal Processing*, **3**, pp. iii–485–488, 2004.

[10] R. E. Carlson and F. N. Fritsch, "Monotone Piecewise Bicubic Interpolation," *SIAM Journal on Numerical Analysis* **22**(2), pp. 386–400, 1985.

[11] K. Martišek and H. Druckmüllerová, "A numerical method for the visualization of the Fe XIV emission in the solar corona using broadband filters," *The Astrophysical Journal Supplement Series* **197**(23), pp. 1–7, 2011.

[12] A. El Gamal, "Trends in CMOS image sensor technology and design," in *IEEE International Electron Devices Meeting*, pp. 805–808, 2002. https://slideplayer.com/slide/5723714/.

[13] C. S. McCamy, H. Marcus, and J. G. Davidson, "A Color-Rendition Chart," *Journal of Applied Photographic Engineering* **2**(3), pp. 95–99, 1976.

[14] M. Stokes, M. Anderson, S. Chandrasekar, and R. Motta, "A Standard Default Color Space for the Internet – sRGB," techreport, Microsoft and Hewlett-Packard, 1996.

[15] C. Poynton, *Digital Video and HD: Algorithms and Interfaces*, The Morgan Kaufmann Series in Computer Graphics, Elsevier, 2012.

[16] G. Sharma and R. Bala, *Digital Color Imaging Handbook*, CRC Press, 2017.

[17] ISO, "Graphic technology – Standard object colour spectra database for colour reproduction evaluation (SOCS)," techreport, International Organization for Standardization, 2003.

JOIN US AT THE NEXT EI!

IS&T International Symposium on

Electronic Imaging

SCIENCE AND TECHNOLOGY

Imaging across applications . . . Where industry and academia meet!

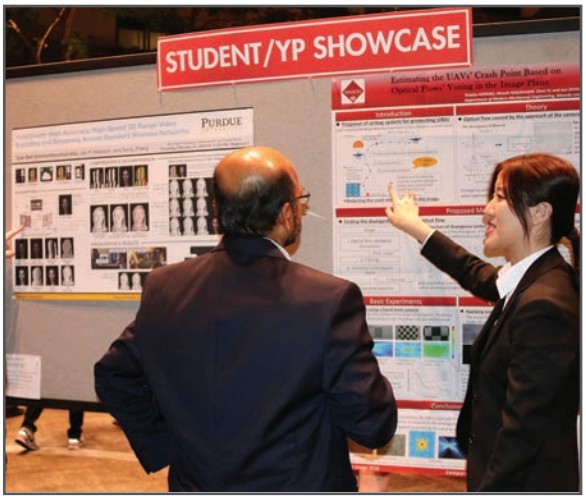

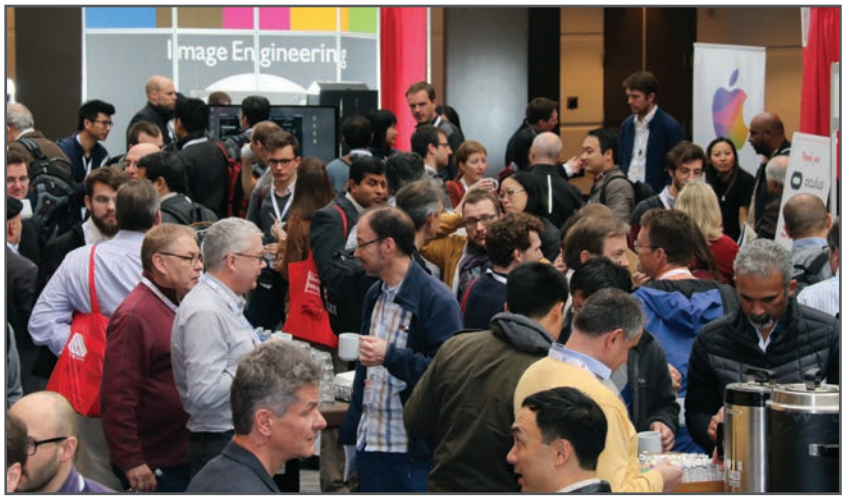

• SHORT COURSES • EXHIBITS • DEMONSTRATION SESSION • PLENARY TALKS •
• INTERACTIVE PAPER SESSION • SPECIAL EVENTS • TECHNICAL SESSIONS •

www.electronicimaging.org

IS&T
imaging.org